Magnetic, charge, and transport properties of graphene nanoflakes

V. S. Protsenko [1,2] and A. A. Katanin [3,1]

[1]*M. N. Mikheev Institute of Metal Physics of Ural Branch of Russian Academy of Sciences,*
S. Kovalevskaya Street 18, 620990 Yekaterinburg, Russia
[2]*Theoretical Physics and Applied Mathematics Department, Ural Federal University, 620002 Yekaterinburg, Russia*
[3]*Center for Photonics and 2D Materials, Moscow Institute of Physics and Technology,*
Institutsky Lane 9, Dolgoprudny, 141700, Moscow Region, Russia

We investigate magnetic, charge, and transport properties of hexagonal graphene nanoflakes (GNFs) connected to two metallic leads by using the functional renormalization group method. The interplay between the on-site and long-range interactions leads to a competition of semimetal (SM), spin-density-wave (SDW), and charge-density-wave (CDW) phases. The ground-state phase diagrams are presented for the GNF systems with screened realistic long-range electron interaction [T. O. Wehling *et al.*, Phys. Rev. Lett. **106**, 236805 (2011)], as well as uniformly screened long-range Coulomb potential $\propto 1/r$. We demonstrate that the realistic screening of Coulomb interaction by σ bands causes moderate (strong) enhancement of critical long-range interaction strength, needed for the SDW (CDW) instability, compared to the results for the uniformly screened Coulomb potential. This enhancement gives rise to a wide region of stability of the SM phase for realistic interaction, such that freely suspended GNFs are far from both SM-SDW and SM-CDW phase-transition boundaries and correspond to the SM phase. Close relation between the linear conductance and the magnetic or charge states of the systems is discussed. A comparison of the results with those of other studies on GNF systems and infinite graphene sheets is presented.

I. INTRODUCTION

Recent progress in the fabrication of nanostructures has allowed reducing the dimension of a graphene plane from a two-dimensional to a zero-dimensional system — the graphene nanoflake (GNF) [1–3]. In addition to being a promising building block for nanoelectronics and spintronic devices [4,5], GNFs are interesting in many aspects from a fundamental point of view. On one hand, the electronic structure of these finite graphene nanostructures can be qualitatively different from that of graphene [4,6]. In particular, due to the appearance of edge states, which do not arise in infinite graphene sheets, the electronic properties of GNFs may depend significantly on the edge geometry [4,6–8]. On the other hand, even small GNF systems with less than 100 atoms demonstrate the occurrence of charge and magnetic instabilities, which are analogous to those of single-layer graphene [9–12].

In an infinite graphene sheet, both short- and long-range electron-electron interactions play an important role, favoring spin-density-wave (SDW) [13–19] or charge-density-wave (CDW) [19–28] correlations. One may expect the same types of correlations to be relevant for GNFs. In particular, GNF clusters of up to 96 sites with on-site U and nearest-neighbor V interactions were investigated in Ref. [9] within the dynamical cluster approximation (DCA). It was found that the competition between short- and long-range interactions gives rise to a nontrivial phase diagram, which includes the transitions between semimetal (SM), SDW, and CDW phases. An increase of U (for $V = 0$) induces a phase transition

from the SM to the SDW state, while a sufficiently large nearest-neighbor interaction V leads to the CDW ground state. At and close to half-filling the transition to the SDW state was also investigated within the dynamic mean-field theory (DMFT) approach for GNF system with 54 atoms coupled to leads [10–12]. The emergence of magnetism in GNF clusters, induced by electron-electron interaction, including the formation of finite magnetic moments, was also predicted within the mean-field [4,8,29,30] and density functional theory (DFT) calculations [8,31,32]. The edge magnetization was thoroughly studied, especially for GNFs with zigzag edges [4,6,31,33–36].

To date, the vast majority of studies on magnetic properties of graphene nanosystems have considered only local and nearest-neighbor electron-electron interactions [37–39]. However, it is well-known that the long-range part of the electron-electron Coulomb interaction is not screened in single-layer graphene. This suggests that the interactions beyond nearest-neighbor distance can also have a crucial impact on the physics of graphene nanosystems, which is confirmed by *ab initio* calculations [40]. Although there are several papers focused on investigating the effects of long-range interaction in graphene nanoflakes beyond the nearest-neighbor interactions [9,34,41–43], most of them are limited to the $1/r$ [41,42] or $1/\sqrt{r^2 + a^2}$ [34] dependence of nonlocal potential on distance r, the parameter a accounts for the finite radius of graphene π orbitals.

At the same time, realistic nonlocal interactions in graphene have been determined by accurate first-principles

calculations [44]. At intermediate distances, this realistic potential differs significantly from the standard Coulomb potential [13,44] due to screening of interaction by σ orbitals. It has been predicted that this difference of the potentials results in the shift of the critical value of the semimetal-insulator phase transition in comparison to the previous estimates [13]. The corresponding position of SDW instability was obtained by the hybrid quantum Monte Carlo (QMC) simulations [13,45,46] and was shown to correspond to the dielectric permittivity $\epsilon < 1$. These considerations show that the magnetic properties of GNFs with the standard bare $1/r$ form of the Coulomb potential may differ significantly from the ones for the realistic model. Thus, it is highly desirable to analyze the competition between different magnetic and charge instabilities in GNFs with the realistic model of nonlocal interactions.

Another important issue is the impact of electron-electron interaction effects on the electron transport of GNF systems. Most studies on this issue are based on either the (dynamic) mean-field or DFT approaches, which do not fully include electron correlation effects. Furthermore, despite the attention paid to the effects inherent to mesoscopic systems in general (e.g., Coulomb blockade [47,48] and quantum interference [11,12,49]), little attention has been focused on the relationship between the electron transport and charge (or spin) correlations in GNF systems (see, e.g., Refs. [34,48]). Understanding this relationship may be important for application of the GNF systems in the development of spin filters and other spintronic devices.

In the present paper, we study the magnetic, charge, and transport properties of hexagonal GNFs of different sizes with realistic nonlocal interaction. The effects of both short- and long-range electron-electron interactions are studied at zero temperature by using the functional renormalization group method. Considering screening of the on-site and nonlocal components of interaction independently we obtain the phase diagrams of the GNFs. We obtain the SDW (CDW) phases at sufficiently strong local (nonlocal) interactions as has been discussed previously. We show that for uniformly screened Coulomb interactions the positions of the obtained instabilities are in agreement with previous studies, but for realistic nonlocal interactions their positions in the phase diagram are somewhat changed. In particular, in the latter case phase diagrams show the presence of a wide region with no instability. Although the position of spin instability for realistic nonlocal interaction was studied previously in Ref. [13] for a sufficiently large graphene sheet, this instability in graphene nanoflakes and the parameters of charge instability for graphene nanoflakes and infinite graphene sheets in the presence of both local and nonlocal interaction to our knowledge were not determined previously. As we argue in the present paper, the CDW instability is more strongly affected by the screening of Coulomb interaction by σ bands than the SDW instability. We also present results for the linear conductance of the GNF systems and clarify features of the conductance associated with the transitions between different magnetic regimes.

The paper is organized as follows. In Sec. II, after presenting the model Hamiltonian for GNF systems we describe the functional renormalization group method. In Sec. III we
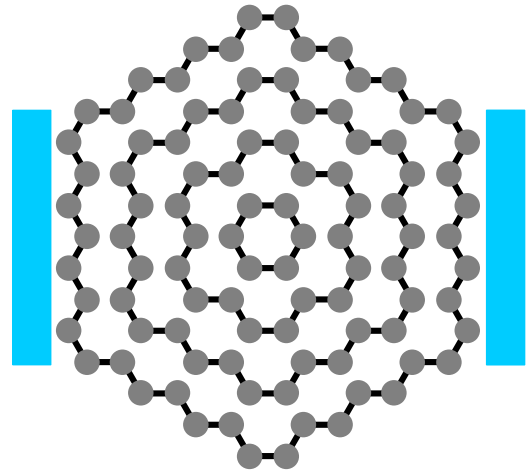

FIG. 1. Zigzag-edge GNF-N systems considered in the paper (regions bounded by closed concentric lines, corresponding to $N = 6$, 24, 54, and 96 from inner to outer line). The left and right leads are shown schematically by rectangles.

consider the results for a purely local interaction, present phase diagrams with account of nonlocal interaction, discuss stability of the CDW and SDW orders, and present results for the linear conductance. Finally, Sec. IV summarizes our main results and presents conclusions.

II. MODEL AND METHOD

We consider systems consisting of graphene nanoflake (GNF-N) with N atoms connected to two metallic leads (see Fig. 1 for zigzag edge geometry). The total Hamiltonian of the GNF-N system can be written as

$$\mathcal{H} = \mathcal{H}_{\text{GNF}} + \mathcal{H}_{\text{leads}} + \mathcal{H}_{\text{T}}. \quad (1)$$

The first term describes the isolated graphene nanoflake,

$$\mathcal{H}_{\text{GNF}} = \sum_{\sigma} \sum_{i \in A} \epsilon_{\sigma}^A n_{i,\sigma} + \sum_{\sigma} \sum_{i \in B} \epsilon_{\sigma}^B n_{i,\sigma} - t \sum_{\langle ij \rangle, \sigma} d_{i,\sigma}^\dagger d_{j,\sigma}$$
$$+ \frac{1}{2} \sum_{i,j} U_{ij}(n_i - 1)(n_j - 1). \quad (2)$$

Here, $d_{i,\sigma}^\dagger$ ($d_{i,\sigma}$) is a creation (annihilation) operator of an electron at the lattice site i of A or B sublattice with a spin index of $\sigma = \pm 1/2$ (or $\sigma = \uparrow, \downarrow$), $n_{j,\sigma} = d_{j,\sigma}^\dagger d_{j,\sigma}$, and $n_j = n_{j,\uparrow} + n_{j,\downarrow}$. The on-site energy parameters are chosen to be $\epsilon_{\sigma}^{A(B)} = \pm(\delta - h\sigma)$, the parameter δ and the magnetic field h are introduced in order to explicitly break the spin and sublattice symmetry of the GNF-N, $t = 2.7$ eV is the nearest-neighbor hopping parameter, and summation in the third term of Eq. (2) is taken over nearest-neighbor sites. The last term in Eq. (2) describes the electron-electron interactions with the potential U_{ij} that includes both on-site $U = U_{ii}$ and nonlocal $U_{i \neq j}$ contributions.

In the following we mainly use the form $U_{i \neq j} = U_{ij}^*/\epsilon_{\text{nl}}$ of the nonlocal interaction, where U_{ij}^* is the realistic nonlocal potential of Ref. [44], which accounts for the screening of Coulomb interaction by σ orbitals. At distances larger than the distance between third-nearest-neighbor lattice sites

$r_{ij} > r_{03} = 2a$ ($a = 0.142$ nm is graphene's lattice constant), the realistic potential is approximated by $U_{ij}^* = 1/(\epsilon_{\rm eff} r_{ij})$ with the effective dielectric permittivity $\epsilon_{\rm eff} = 1/(U_{03}^* r_{03}) \approx 1.41$, as in Ref. [13]. In this case, independent variation of the parameters U and $\epsilon_{\rm nl}$ allows us to study the interplay between the on-site and the nonlocal parts of the interactions. According to Ref. [44], $U = U_r = 9.3$ eV$\approx 3.44t$ corresponds to the realistic on-site interaction in graphene.

The second part $\mathcal{H}_{\rm leads}$ of the Hamiltonian (1) describes the two equivalent metallic leads,

$$\mathcal{H}_{\rm leads} = \sum_{k,\alpha,\sigma} \epsilon_k c_{k,\alpha,\sigma}^\dagger c_{k,\alpha,\sigma}. \tag{3}$$

Here, $c_{k,\alpha,\sigma}^\dagger$ ($c_{k,\alpha,\sigma}$) is a creation (annihilation) operator of an electron with the state k and spin σ in the left ($\alpha = L$) or right ($\alpha = R$) lead, and ϵ_k represents the single-particle energy.

The last term in Eq. (1) describes the connection between the GNF-N and the leads, following Ref. [11] we consider it in the form

$$\mathcal{H}_{\rm T} = -\sum_{\sigma,k,\alpha,i_\alpha} (V_{i_\alpha,k,\alpha} c_{k,\alpha,\sigma}^\dagger d_{i_\alpha,\sigma} + {\rm H.c.}), \tag{4}$$

where $V_{i,k,\alpha}$ is the coupling matrix element between the ith site of GFN-N and the kth state of the lead α, and summation is performed over sites i_α that are closest to the lead α.

To reveal the formation of SDW and CDW phases of GNF-N we calculate the average relative staggered magnetization,

$$S_{\rm st} = (\langle N_{A,\uparrow}\rangle + \langle N_{B,\downarrow}\rangle - \langle N_{A,\downarrow}\rangle - \langle N_{B,\uparrow}\rangle)/N, \tag{5}$$

and the average relative difference between the occupation of A and B sublattices,

$$\Delta_{\rm st} = (\langle N_{B,\uparrow}\rangle + \langle N_{B,\downarrow}\rangle - \langle N_{A,\uparrow}\rangle - \langle N_{A,\downarrow}\rangle)/N, \tag{6}$$

which have a maximal value of 1, $\langle N_{A(B),\sigma}\rangle = \sum_{i\in A(B)} \langle n_{i,\sigma}\rangle$. It is worth noting that due to the particle-hole symmetry of the Hamiltonian (2) the total average occupation of the GNF-N is automatically fixed to half-filling, $\sum_\sigma(\langle N_{A,\sigma}\rangle + \langle N_{B,\sigma}\rangle) = N$ even in presence of electron-electron interactions. The average occupation of a lattice site i for spin σ can be calculated at temperature $T = 0$ as

$$\langle n_{j,\sigma}\rangle = \int \frac{d\omega}{2\pi} e^{i\omega 0^+} \mathcal{G}_{jj,\sigma}(i\omega). \tag{7}$$

Here $\mathcal{G}(i\omega)$ is the Green's function corresponding to the Hamiltonian (1) projected onto the states of GNF-N.

To determine the Green's function $\mathcal{G}(i\omega)$ we use the functional renormalization group (fRG) technique [50–52]. This technique introduces the cutoff parameter Λ, specified below in Eq. (19), such that the physical Green's function is obtained in the end of the fRG flow, i.e., for the corresponding cutoff parameter $\Lambda = 0$, $\mathcal{G}(i\omega) = \mathcal{G}^{\Lambda=0}(i\omega)$. By using the Dyson equation and the projection technique, the cutoff-dependent Green's function $\mathcal{G}^\Lambda(i\omega)$ can be written as

$$\mathcal{G}^\Lambda(i\omega) = \{[\mathcal{G}_0^\Lambda(i\omega)]^{-1} - \Sigma_{\rm leads} - \Sigma^\Lambda\}^{-1}, \tag{8}$$

where $\mathcal{G}_0^\Lambda(i\omega)$ is the cutoff-dependent bare Green's function, $\Sigma_{\rm leads}$ describes the coupling between the GNF-N and the leads, and Σ^Λ is the self-energy of the interacting ($U_{ij} \neq 0$)

system. Following Ref. [11], for $\Sigma_{\rm leads}$ we take into account only diagonal (with respect to site indices) hybridization processes and use the wide band limit approximation [53]. This leads to $\Sigma_{\rm leads} = -i\Gamma{\rm sign}(\omega)$ for each site of the GNF-N connected to leads, where $\Gamma \propto |V|^2\rho_{\rm lead}$ is an energy-independent hybridization strength and $\rho_{\rm lead}$ is the density of states in the leads.

The self-energy Σ^Λ can be obtained from an infinite hierarchy of differential flow equations for the cutoff-parameter-Λ-dependent self-energy Σ^Λ and the n-particle vertices Γ_{2n}^Λ, $n \geqslant 2$ [50,51]. Truncating the fRG flow equations by neglecting the flow of the vertex functions with $n \geqslant 3$ and discarding the frequency dependence of vertices leads to a closed system of the flow equations for Σ^Λ and the two-particle vertex Γ_4^Λ [51,52].

In the present study, we use the coupled-ladder approximation [54,55] to this closed set of fRG equations, which makes numerical calculations feasible for the systems under consideration. This approximation consists of decomposition of the two-particle vertex Γ_4^Λ into the particle-particle (P^Λ), the exchange particle-hole (X^Λ), and the direct particle-hole (D^Λ) channels,

$$\begin{aligned} \Gamma_4^\Lambda(j_1', j_2', j_1, j_2, \boldsymbol{\sigma}) &= I(j_1', j_2', j_1, j_2, \boldsymbol{\sigma}) \\ &+ P^\Lambda(j_1', j_1, \boldsymbol{\sigma})\delta_{j_1'j_2'}\delta_{j_1j_2} \\ &+ X^\Lambda(j_1, j_2, \boldsymbol{\sigma})\delta_{j_1'j_1}\delta_{j_2'j_2} \\ &+ D^\Lambda(j_2, j_1, \boldsymbol{\sigma})\delta_{j_2'j_1}\delta_{j_1'j_2}, \end{aligned} \tag{9}$$

and splitting the flow equation for the two-particle vertex Γ_4^Λ into the equations for these individual channels. Term I in Eq. (9) is the antisymmetrized bare interaction and $\boldsymbol{\sigma} = (\sigma_1', \sigma_2', \sigma_1, \sigma_2)$ is a multi-index. The fRG equations for the self-energy Σ^Λ and for the vertices P^Λ, X^Λ, and D^Λ can be written in the following forms:

$$\partial_\Lambda \Sigma^\Lambda = -\int \frac{d\omega}{2\pi} e^{i\omega 0^+} \mathcal{S}^\Lambda(i\omega) \circ \Gamma_4^\Lambda, \tag{10}$$

$$\partial_\Lambda P^\Lambda = \int \frac{d\omega}{2\pi} \Gamma_p^\Lambda \circ \mathcal{S}^\Lambda(i\omega) \circ \mathcal{G}^\Lambda(-i\omega) \circ \Gamma_p^\Lambda, \tag{11}$$

$$\begin{aligned} \partial_\Lambda X^\Lambda = -\int \frac{d\omega}{2\pi} \Gamma_x^\Lambda \circ [\mathcal{S}^\Lambda(i\omega) \circ \mathcal{G}^\Lambda(i\omega) \\ + \mathcal{G}^\Lambda(i\omega) \circ \mathcal{S}^\Lambda(i\omega)] \circ \Gamma_x^\Lambda, \end{aligned} \tag{12}$$

$$\begin{aligned} \partial_\Lambda D^\Lambda = \int \frac{d\omega}{2\pi} \Gamma_d^\Lambda \circ [\mathcal{S}^\Lambda(i\omega) \circ \mathcal{G}^\Lambda(i\omega) \\ + \mathcal{G}^\Lambda(i\omega) \circ \mathcal{S}^\Lambda(i\omega)] \circ \Gamma_d^\Lambda, \end{aligned} \tag{13}$$

where

$$\Gamma_p^\Lambda(j_1, j_2, \boldsymbol{\sigma}) = P^\Lambda(j_1, j_2, \boldsymbol{\sigma}) + I(j_1, j_1, j_2, j_2, \boldsymbol{\sigma}), \tag{14}$$

$$\Gamma_x^\Lambda(j_1, j_2, \boldsymbol{\sigma}) = X^\Lambda(j_1, j_2, \boldsymbol{\sigma}) + I(j_1, j_2, j_1, j_2, \boldsymbol{\sigma}), \tag{15}$$

$$\Gamma_d^\Lambda(j_1, j_2, \boldsymbol{\sigma}) = D^\Lambda(j_1, j_2, \boldsymbol{\sigma}) + I(j_1, j_2, j_2, j_1, \boldsymbol{\sigma}), \tag{16}$$

for $j_1 \neq j_2$, and

$$\begin{aligned} \Gamma_f^\Lambda(j_1, j_1, \boldsymbol{\sigma}) = P^\Lambda(j_1, j_1, \boldsymbol{\sigma}) + X^\Lambda(j_1, j_1, \boldsymbol{\sigma}) \\ + D^\Lambda(j_1, j_1, \boldsymbol{\sigma}) + I(j_1, j_1, j_1, j_1, \boldsymbol{\sigma}) \end{aligned} \tag{17}$$
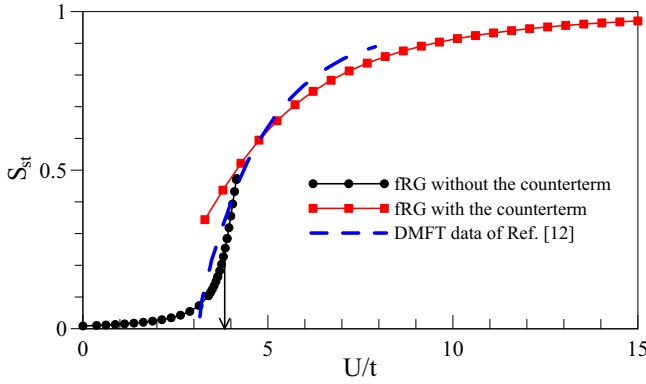
FIG. 2. The average relative staggered magnetization S_{st} as a function of U/t for the GNF-54 system with $U_{i \neq j} = 0$. The square (circle) symbols correspond to the fRG results with (without) the counterterm. The dashed line represents the DMFT data of Ref. [12]. The arrow indicates $U = U_c^{54} \approx 3.83t$ corresponding to $S_{st} = 1/4$.

for $j_1 = j_2$, $f = p$, x, and d. In Eqs. (10)–(13) $\mathcal{S}^\Lambda$ is the single-scale propagator

$$\mathcal{S}^\Lambda = \mathcal{G}^\Lambda \partial_\Lambda (\mathcal{G}_0^\Lambda)^{-1} \mathcal{G}^\Lambda, \tag{18}$$

and "∘" denotes summations over intermediate site and spin indexes, which perform according to the standard diagrammatic rules.

To introduce the cutoff parameter Λ we use the reservoir cutoff scheme [56] in the form

$$\mathcal{G}_0^\Lambda (i\omega) = \left[\mathcal{G}_0^{-1}(i\omega) + iI_N \Lambda \,\mathrm{sign}(\omega) \right]^{-1}, \tag{19}$$

where I_N is the $N \times N$ identity matrix, and $\mathcal{G}_0(i\omega)$ is the bare Green's function, corresponding to the single-particle part of the Hamiltonian (2) (i.e., $\mathcal{H}_{GNF}$ with $U_{ij} = 0$). The value of Σ^Λ obtained at the end of the fRG flow (for $\Lambda \to 0$) corresponds to the physical self-energy Σ of the interacting system.

The linear conductance $G = e^2/h \sum_\sigma \mathcal{T}_\sigma(\omega \to 0)$ at $T = 0$, where the transmission function $\mathcal{T}_\sigma(\omega)$ in our case can be written in the form [11,12]

$$\mathcal{T}_\sigma(\omega) = 4\Gamma^2 \sum_{i,j} \left| \mathcal{G}_{ij,\sigma}^r(\omega) \right|^2. \tag{20}$$

Here $\mathcal{G}^r(\omega) = \mathcal{G}^{\Lambda=0}(i\omega \to \omega + i0^+)$ is the retarded Green's function of the GNF-N and summation over the site indexes i (j) is restricted to sites of GNF-N connected to the left (right) lead. Note that Eq. (20) assumes that only local hybridization processes affect the transmission [11].

III. RESULTS

In the following calculations we set $\delta = 0.0185t$, $\Gamma = 0.02t$, $T = 0$, and, unless otherwise stated, $h = \delta$.

A. Zigzag-edge GNF-N with purely local interaction

Let us first consider the zigzag-edge GNF-N systems with a purely local (on-site) interaction U, when $U_{i \neq j} = 0$. In Fig. 2, the fRG results for the average relative staggered magnetization S_{st} are shown for the GNF-54 system. In the limit
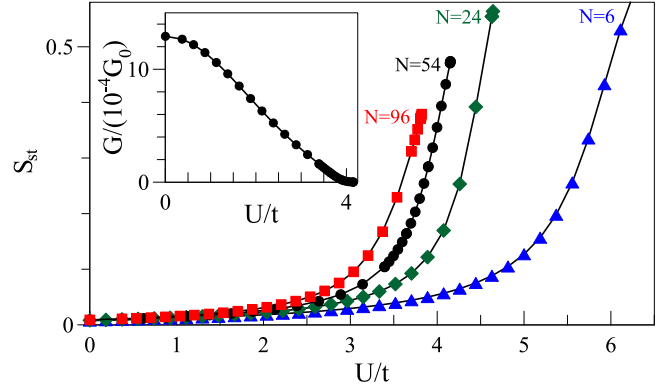

FIG. 3. The average relative staggered magnetization S_{st} as a function of U/t for the GNF-N systems with $U_{i \neq j} = 0$ and $N = 6$ (blue triangles), $N = 24$ (green diamonds), $N = 54$ (black circles), and $N = 96$ (red squares). Inset: The linear conductance G as a function of U/t for the GNF-54 system with $U_{i \neq j} = 0$; $G_0 = e^2/h$ is the conductance quantum per spin projection.

$U \ll t$, the magnetization of the GNF-N system is small but nonzero due to the presence of the finite magnetic field. With increasing U/t, the magnetization increases monotonously, indicating the formation of the SDW order. For sufficiently large U/t, the vertices obtained from fRG equations diverge.

Similarly to Ref. [57] we have found that the convergence of the vertices obtained from fRG equations can be achieved by applying the counterterm technique. The counterterm (which corresponds in our case to introducing the auxiliary magnetic field $\tilde{h} = 1.5t$, switched off linearly with Λ starting from the scale $\Lambda_c = 0.1t$) allows us to continue the $S_{st}(U/t)$ dependence beyond the point at which the fRG approach without the counterterm breaks down (see Fig. 2). However, for smaller U/t the fRG results with and without the counterterm are different from each other. Apparently, this is due to the unphysical spin-splitting of the self-energy in the fRG approach with a counterterm, which does not allow us to correctly reproduce the SM state of the system. In Fig. 2 we also compare fRG results to the DMFT results of Ref. [12] in the absence of a magnetic field. One can see that for substantial (small) S_{st} the fRG approach with (without) the counterterm provides a reasonable agreement with the DMFT data of Ref. [12]. Since we are interested in the position of phase transitions to SDW (CDW) phases, rather than in the study of the regions deep inside these phases, in the following we restrict ourselves to the fRG approach without the counterterm.

Figure 3 shows the average relative staggered magnetization S_{st} as a function of U/t for a series of GNF-N systems of different sizes. In our case of a finite small magnetic field, which is introduced to break explicitly the spin symmetry, the transition from the SM ($S_{st} \to 0$) to the SDW ($S_{st} \approx 1$) phase is smoothed. To find the position of the phase transition between the SM and SDW phases we define a characteristic local interaction U_c^N of the GNF-N by the value U corresponding to a quarter of the maximum sublattice magnetization, $S_{st} = 1/4$. We assume that in view of sharpness of the dependence S_{st} on U near the magnetic phase transition for not very small nanoflakes, the obtained values of interactions U_c^N are close

TABLE I. Estimates of characteristic local interaction U_c^N/t, corresponding to $S_{st} = 0.25$.

N	6	24	54	96
U_c^N/t	5.54	4.25	3.83	3.59

to the critical interaction for the magnetic transition in the limit $h \to 0$. The obtained characteristic interactions U_c^N/t are presented in Table I. The obtained value of U_c^N agrees well with the result of the DMFT approach for $N = 54$ [12], $U_c \approx 3.6t$ (obtained from the condition $S_{st} = 1/4$), and the result of the DCA approach for $N = 96$, $U_c \lesssim 3.6t$ [9] (obtained from vanishing sublattice magnetization).

Finally, in the inset of Fig. 3, we show the linear conductance G as a function of U/t for the GNF-54 system. With the increase of U/t (and hence S_{st}), the conductance gradually decreases. When $U \gtrsim U_c^{54}$, the SDW order is developed and the conductance is suppressed. The other GNF-N systems under consideration produce qualitatively similar behavior of the conductance.

B. Zigzag-edge GNF-N with account of nonlocal interaction

We next study the zigzag-edge GNF-N systems with both on-site (U) and nonlocal ($U_{i \neq j} = U_{i \neq j}^*/\epsilon_{nl}$) electron-electron interactions.

In Fig. 4, we plot S_{st} as a function of U/t for the GNF-54 system for various values of the screening parameter of the nonlocal interaction ϵ_{nl}. In the case of $\epsilon_{nl} \gg 1$, the magnetization tends to that for the case when only on-site interaction is present. With decreasing ϵ_{nl}, the region with nonzero magnetization shifts to the higher values of U/t. The example of spin distribution at sufficiently large U in the symmetry-broken phase is shown in Fig. 5. The spin distribution is qualitatively analogous to the one presented for the purely local interaction ($\epsilon_{nl}^{-1} = 0$) case in Ref. [12]. The other systems show similar behavior of S_{st} with respect to both U/t and ϵ_{nl}.

Figure 6 shows the average relative difference between the occupation of the sublattices Δ_{st} and the average relative stag-
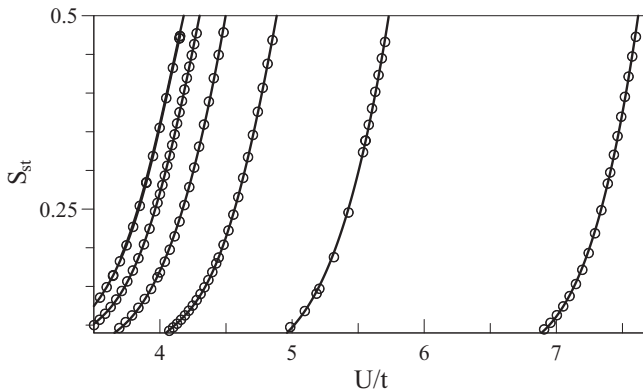

FIG. 5. The distribution of the magnetization $m_j = |\langle n_{j,\uparrow} - n_{j,\downarrow}\rangle|$ in the GNF-54 system with $U = 11$ eV $\approx 4.07t > U_c^{54}$ and $\epsilon_{nl} = 7$. The red (blue) dots correspond to A (B) sublattices; their size is proportional to m_j. The open circles indicate the sites corresponding to the max$\{m_j\} \approx 0.36$. The relative average staggered magnetization $S_{st} \approx 0.28$.

gered magnetization S_{st} as a function of ϵ_{nl}, for the GNF-54 system with $U = 11$ eV $\approx 4.07t$. When the magnetization S_{st} is almost suppressed, Δ_{st} increases monotonously with decreasing ϵ_{nl}. In the limit $\epsilon_{nl} \ll 1$ we have $\Delta_{st} \approx 1$ and $S_{st} \approx 0$, which correspond to the CDW order of the system. The establishing of the CDW order for $\epsilon_{nl} \lesssim 1$ is clearly seen from the checkerboard distribution of $\langle n_j \rangle = \langle n_{j,\uparrow} + n_{j,\downarrow} \rangle$ (see, e.g., Fig. 7). In particular, for $\epsilon_{nl} = 0.3$ we have $\langle n_{j \in B} \rangle \approx 2$ and $\langle n_{j \in A} \rangle \approx 0$ for the GNF-54 system. Thus, the decrease of ϵ_{nl}, which corresponds to the increase of the long-range interaction, drives the phase transition from the SM state ($S_{st} \approx 0$, $\Delta_{st} \approx 0$) to the CDW one ($S_{st} \approx 0$, $\Delta_{st} \approx 1$). We find that the SM-CDW phase transition takes place for all GNF-N systems and an arbitrary value of on-site interaction U parameter (including $U = 0$ case), while the SM-SDW one occurs for $U > U_c^N$.

To obtain the SM-SDW phase boundaries, we again define the characteristic U/t for fixed ϵ_{nl} as the value corresponding to $S_{st} = 1/4$. The resulting dependence of the inverse critical

FIG. 4. The average relative staggered magnetization S_{st} of the GNF-54 system as a function of U/t for various ϵ_{nl}. From right to left: $\epsilon_{nl} = 0.5$, 1, 2, 4, and 9.8, and $\epsilon_{nl}^{-1} = 0$ ($U_{i \neq j} = 0$ in the latter case). The solid lines are fourth-order polynomial interpolation of the fRG data.
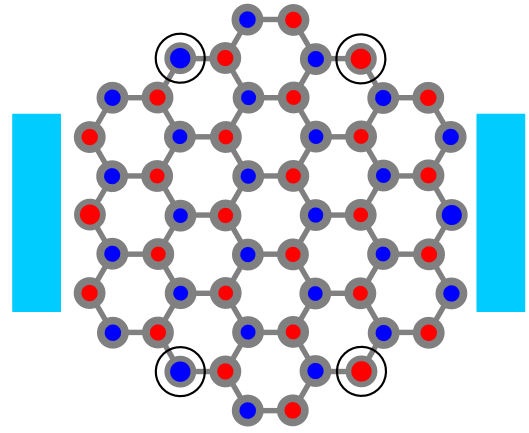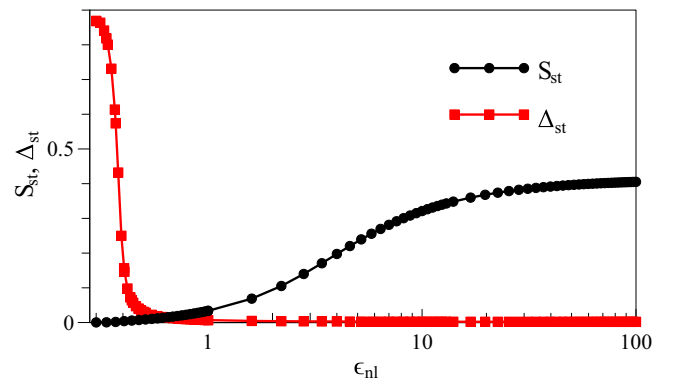

FIG. 6. The average relative staggered magnetization S_{st} (black circles) and the average relative difference in occupation of the sublattices Δ_{st} (red squares) as a function of ϵ_{nl} (in logarithmic scale) for the GNF-54 system with $U = 11$ eV $\approx 4.07t$.
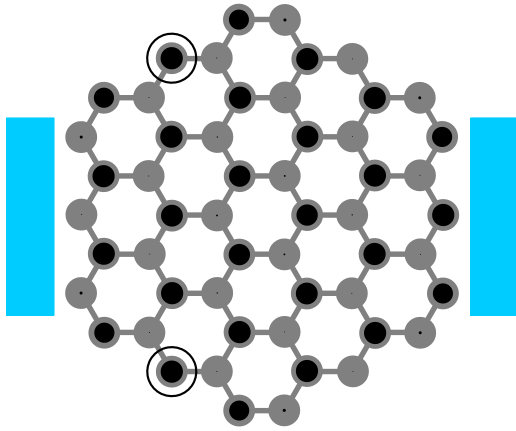
FIG. 7. The distribution of $\langle n_j \rangle = \langle n_{j,\uparrow} + n_{j,\downarrow} \rangle$ for the GNF-54 system with $U = 11$ eV $\approx 4.07t$ and $\epsilon_{\text{nl}} = 0.3$. The size of the black dots is proportional to $\langle n_j \rangle$. The open circles indicate the sites corresponding to the max$\{\langle n_j \rangle\} \approx 1.92$.

screening $\epsilon_{\text{nl}}^{-1}$ and the corresponding graphene's "fine structure" constant $\alpha_0 = e^2/(\epsilon_{\text{nl}}\epsilon_{\text{eff}} v_F^0)$, where $v_F^0 = 3at/2$ is the bare Fermi velocity, on the obtained values of U/t are shown in Fig. 8. For $\epsilon_{\text{nl}} \gg 1$ the long-range part of the nonlocal potential is small and the on-site interaction U plays the main role. In this limit, the on-site interaction $U \gtrsim U_c^N$ (as for the $\epsilon_{\text{nl}}^{-1} = 0$ case) leads to the SDW order of the systems. When ϵ_{nl} is sufficiently small, the SDW state becomes unstable and the SM state occurs for all GNF-N systems. With increase of
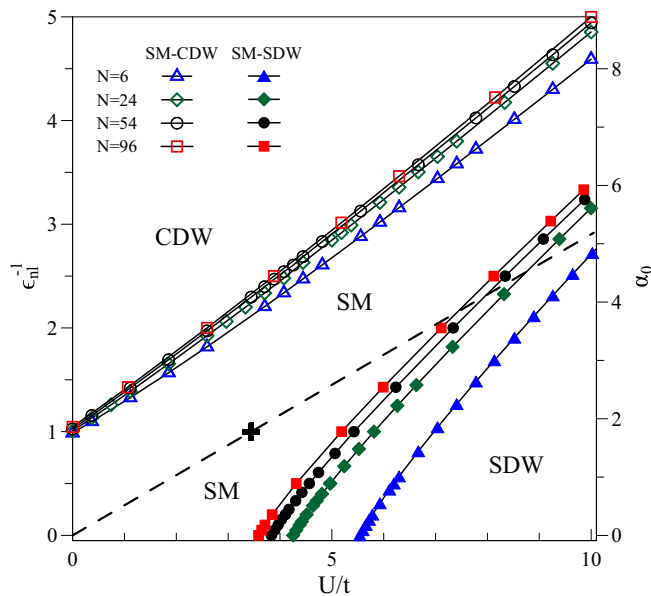

FIG. 8. Phase diagram of the zigzag-edge GNF-N system in the $(U/t, \epsilon_{\text{nl}}^{-1})$ and $(U/t, \alpha_0)$ coordinates for $N = 6$ (blue triangles), $N = 24$ (green diamonds), $N = 54$ (black circles), and $N = 96$ (red squares): SM-SDW phase transitions are denoted by solid lines with solid symbols, and SM-CDW phase transitions are marked by solid lines with open symbols. The dashed line $U = U_r/\epsilon_{\text{nl}}$ corresponds to simultaneous rescaling of the on-site and long-range part, considered in Ref. [13]. The point $\epsilon_{\text{nl}} = 1$ and $U = 9.3$ eV $\approx 3.4t$, corresponding to freely suspended graphene, is marked by the plus symbol.

the size of the system N, the critical value of the parameter ϵ_{nl} decreases.

Analogously to the case of the SM-SDW phase transition, we define the SM-CDW phase boundary as the line $\epsilon_{\text{nl}}^{-1}(U/t)$ at which $\Delta_{\text{st}} = 1/4$. Our results for the SM-SDW and SM-CDW phase-transition lines for different GNF-N systems are also summarized in Fig. 8. For $U < U_c^N$, the GNF-N system undergoes the phase transition from the SM to the CDW ground state induced by changing the ϵ_{nl} parameter. When $U > U_c^N$, the SDW phase occurs and with increasing ϵ_{nl} from value $\epsilon_{\text{nl}} = 0$ the system undergoes two phase transitions: first, from the CDW to the SM phase and, second, from the SM to the SDW phase. The calculated SM-CDW phase transition lines $\epsilon_{\text{nl}}^{-1}(U/t)$ are very close to each other (except the $N = 6$ case) and are well approximated by linear dependencies.

The important feature of the phase diagram of Fig. 8 is a strong increase of the critical α_0 of charge instability with an increase of U. As a result, in contrast to the case of on-site and nearest-neighbor interaction [9,58], there is a wide region of the phase diagram with no instability. The GNF-N system with the realistic nonlocal interaction (for $U = U_r$ and $\epsilon_{\text{nl}} = 1$) falls into this region and, therefore, corresponds to the SM ground state of the system (marked with the plus symbol in Fig. 8). Moreover, as can be seen from Fig. 8, all considered GNF-N systems with $\epsilon_{\text{nl}} > 1$ are far from both SM-SDW and SM-CDW phase-transition lines.

To provide an insight into the importance of screening of nearest- and next-nearest-neighbor Coulomb interactions by σ bands, which yields the difference of the considered nonlocal potential U_{ij}^* of Refs. [13,44] from the bare Coulomb interaction, in Fig. 9 we compare the above-discussed fRG results to the results for the uniformly screened Coulomb interaction $U_{i\neq j} = e^2/(\epsilon_{\text{nl}}\epsilon_{\text{eff}} r_{ij})$. One can see that realistic screening of the Coulomb interaction, having smaller nearest- and next-nearest-neighbor interaction, only moderately increases the critical constant α_0 for the SDW instability, but strongly enhances critical nonlocal interaction for the charge instability. Without this enhancement, freely suspended graphene nanoflakes (as well as an infinite graphene sheet) would be on the verge of the charge instability. Although this effect was qualitatively discussed previously in Ref. [13], the position of only spin, and not charge instability, with account of screening effects was analyzed in that study. The obtained critical nonlocal interaction of the charge density wave at $U = 0$ for the GNF-96 system corresponds to $\epsilon_{\text{nl}} \approx 0.96$, i.e., $\alpha_0 \approx 1.86$ for realistic nonlocal interaction and $\epsilon_{\text{nl}} \approx 2.32$, i.e., $\alpha_0 \approx 0.77$ for uniformly screened interaction. The latter value is not far from the critical $\alpha_0 \simeq (0.9-1.1)$ for charge instability in an infinite plane, obtained by QMC in Ref. [24] and mean-field approximation with dynamic renormalized Coulomb interaction [25,26].

For realistic nonlocal interaction the SDW instability of the GNF is reached along the line $U = U_r/\epsilon_{\text{nl}}$, corresponding to simultaneous rescaling of the on-site and nonlocal interaction, $U_{ij} = U_{ij}^*/\epsilon$, and the parameter $\epsilon = \epsilon_{\text{nl}}$ can be viewed as the dielectric permittivity of the medium surrounding the GNF. The crossing of the boundary of SDW instability with this line corresponds for the GNF-96 system to the physically unreachable value of $\epsilon = 0.46$, which is very close to that
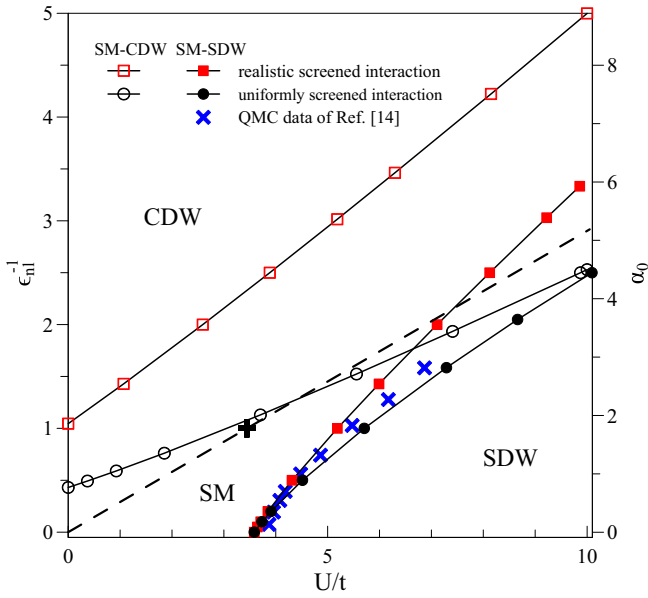
FIG. 9. Critical ϵ_{nl}^{-1} and corresponding fine-structure constant $\alpha_0 = e^2/(\epsilon_{nl}\epsilon_{eff} v_F^0)$ for SM-SDW (solid lines with solid symbols) and SM-CDW (solid lines with open symbols) phase transitions as functions of U/t for the GNF-96 system with the realistic screened $U_{i\neq j} = U_{ij}^*/\epsilon_{nl}$ (red squares) and the uniformly screened $U_{i\neq j} = e^2/(\epsilon_{nl}\epsilon_{eff} r_{ij})$ (black circles) form of nonlocal interaction. The blue crosses are data obtained from scaling analysis of QMC results in Ref. [14]. The dashed line $U = U_r/\epsilon_{nl}$ corresponds to simultaneous screening of local and nonlocal interaction. The point $\epsilon_{nl} = 1$ and $U = 9.3$ eV $\approx 3.4t$, corresponding to freely suspended graphene, is marked by the plus symbol.

for the infinite sheet, obtained in Ref. [13] (see Ref. [59]). At the same time, for uniformly screened interaction the SDW instability is not obtained at all along the same path. The result for the critical interaction constant $\alpha_0(U/t)$ for the GNF-96 system, corresponding to SDW instability for uniformly screened Coulomb interaction, is also compared in Fig. 9 to that from QMC analysis in large systems [14,60]. The obtained fRG result provides quantitative agreement with the scaling analysis of QMC data.

In Fig. 10 the linear conductance G of the GNF-54 system at $T = 0$ is plotted as a function of ϵ_{nl}. For strong nonlocal interaction ($\epsilon_{nl} \ll 1$) the conductance is suppressed due to formation of the CDW. For $U > U_c^{54} \approx 3.8t$ (see for, e.g., the plot $G(\epsilon_{nl})$ for $U = 11$ eV $\approx 4.07t$), the conductance is suppressed also for weak ($\epsilon_{nl} \gg 1$) nonlocal interaction due to the development of the SDW order. In the latter case at some intermediate ϵ_{nl} at which $S_{st}, \Delta_{st} \approx 0$ (see Fig. 6), the conductance has a maximum. When $U \lesssim U_c^{54}$ the SDW phase does not occur and the peak in the conductance gradually disappears with decreasing U, such that G becomes a monotonous function of ϵ_{nl}. In the latter case, opposite to the $U > U_c^{54}$ case, the conductance tends to a nonzero value in the limit $\epsilon_{nl} \gg 1$. We have found that the above behavior of the conductance is generic for all GNF-N systems under consideration.

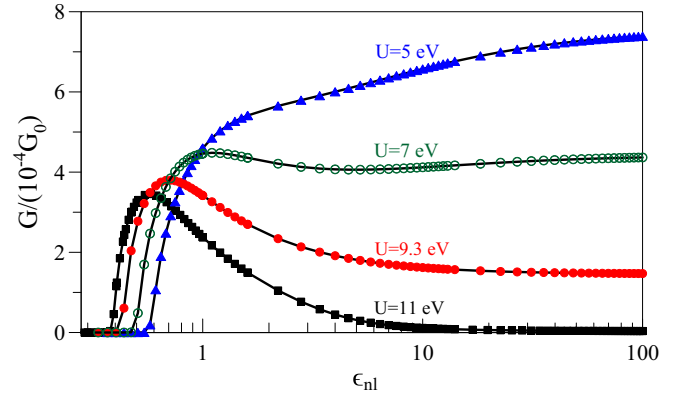Finally, in Fig. 11 we show the magnetic field dependence of the average relative staggered magnetization S_{st} and

the linear conductance G of the GNF-54 and GNF-96 systems with the realistic nonlocal potential ($U = U_r$, $\epsilon_{nl} = 1$). For both systems and small magnetic fields $h \lesssim 0.02t$, the sublattice magnetization is well fitted by the linear function $S_{st}(h) = \chi^N h$, which confirms the SM nature of the GNFs for

FIG. 10. The linear conductance G as a function of ϵ_{nl} (in logarithmic scale) for the GNF-54 system with $U = 5$ eV $\approx 1.85t$ (blue triangles), $U = 7$ eV $\approx 2.6t$ (dark green open circles), $U = 9.3$ eV $\approx 3.44t$ (red solid circles), and $U = 11$ eV $\approx 4.07t$ (black squares).
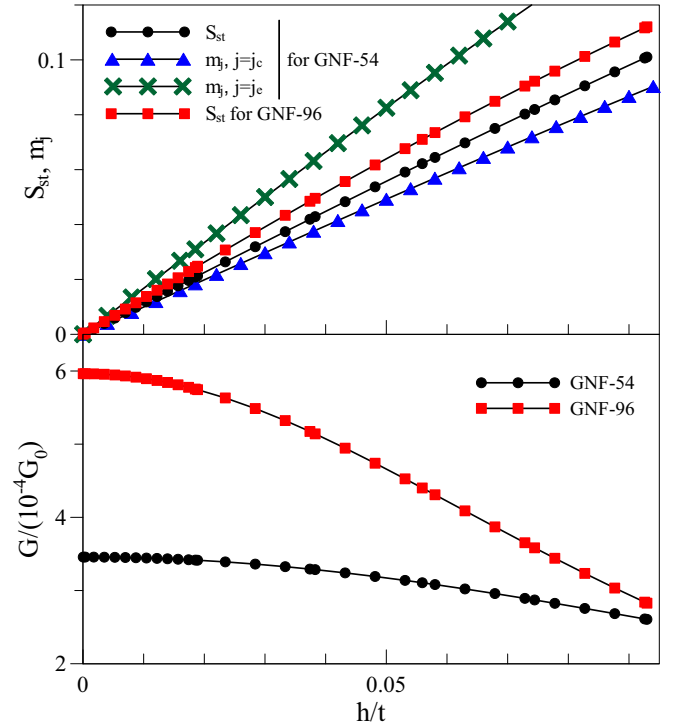

FIG. 11. Upper part: The average relative staggered magnetization S_{st} for the GNF-54 (black circles) and GNF-96 (red squares) systems, together with the magnetization of the GNF-54 system $m_j = |\langle n_{j,\uparrow} - n_{j,\downarrow}\rangle|$ at the center site j_c (blue triangles) and at the center of edge j_e (green crosses) as a function of h/t. Lower part: The linear conductance G as a function of h/t for the GNF-54 (black circles) and GNF-96 (red squares) systems. The realistic nonlocal potential ($U = U_r$, $\epsilon_{nl} = 1$) is considered.
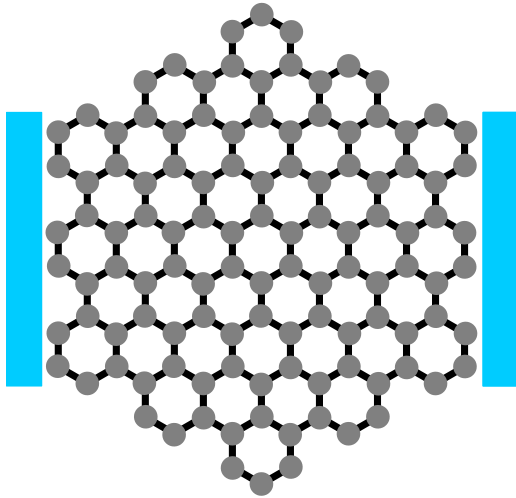
FIG. 12. Armchair-edge GNF system with $N = 114$. The left and right leads are shown schematically by rectangles.

the realistic parameters. The parameter χ^N can be considered as the paramagnetic susceptibility. We find $\chi^{54} \approx 1.13/t$ and $\chi^{96} \approx 1.32/t$ for the GNF-54 system and the GNF-96 system, respectively, which corresponds to a paramagnetic state, albeit with pronounced spin correlations. To characterize the distribution of spin order in a finite magnetic field, we also present the results for the absolute value of the magnetization $m_j = |\langle n_{j,\uparrow} - n_{j,\downarrow} \rangle|$ at the center site j_c and at the center of edge j_e of the GNF-54 system. One can see that the magnetization at the edge is substantially larger than that in the center and also substantially different from the staggered relative magnetization S_{st}, due to formation of the edge states. The linear conductance G depends monotonously on the magnetic field and becomes almost constant for relatively small magnetic fields ($h/t \lesssim 0.02$).

C. Comparison to armchair GNFs

In the following we compare the obtained results to those for the armchair-edge GNFs with $N = 42$ and $N = 114$ atoms (see Fig. 12). To define the SM-CDW and SM-SDW phase-transition lines for armchair-edge GNFs we use the same procedure as in Sec. III B. The corresponding lines of phase transitions for these systems are presented and compared to the zigzag-edge GNF-54 system in Fig. 13. The position of the SM, CDW, and SDW phases in the $(U/t, \epsilon_{nl}^{-1})$ coordinates remains qualitatively the same as in the case of zigzag-edge GNFs. Furthermore, as for the zigzag-edge GNFs with $N > 6$ (see Fig. 8) the SM-SDW (SM-CDW) phase-transition lines for GNFs with armchair edges are (very) close to each other even if the N values are substantially different. However, for fixed U both SDW and CDW phase transitions for armchair GNFs take place at somewhat smaller values of nonlocal interaction (higher ϵ_{nl}) than the corresponding transitions in zigzag-edge GNFs with close N. For example, the SM-SDW phase-transition line for the armchair-edge $N = 114$ system is quantitatively closer to the one for the zigzag-edge GNF-54 system rather than to the one obtained for the zigzag-edge GNF-96 system.
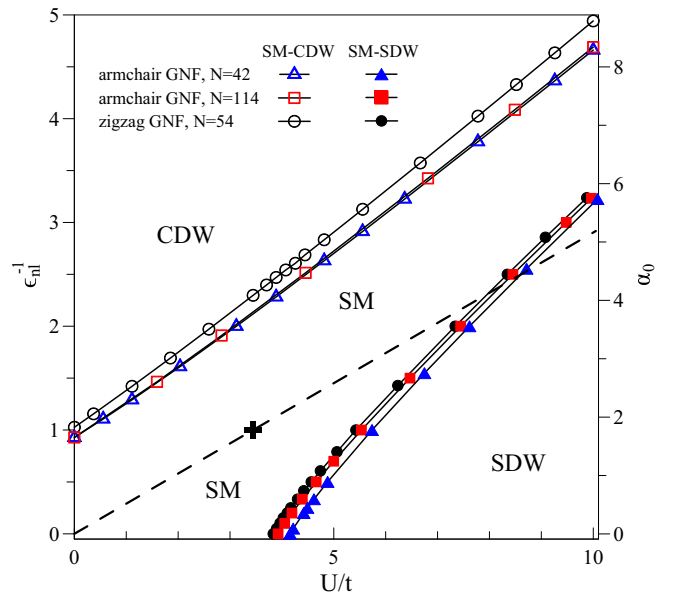

FIG. 13. Phase diagrams for the armchair-edge GNF-42 (blue triangles) and armchair-edge GNF-114 (red squares) systems, compared to the zigzag-edge GNF system with $N = 54$ (black circles): SM-SDW phase transitions are denoted by solid lines with solid symbols, and SM-CDW phase transitions are marked by solid lines with open symbols. The dashed line $U = U_r/\epsilon_{nl}$ corresponds to simultaneous rescaling of the on-site and long-range part, considered in Ref. [13]. The point $\epsilon_{nl} = 1$ and $U = 9.3$ eV $\approx 3.4t$, corresponding to freely suspended graphene, is marked by the plus symbol.

The conductance for the armchair-edge geometry (not shown) is reduced by about an order of magnitude compared to the conductance of zigzag-edge systems with close size. This stresses importance of interference effects for GNF conductance. However, the general relations between the conductance and the magnetic states of the GNF systems revealed in the present study are preserved also for an armchair-edge geometry.

IV. CONCLUSION

In this paper, we have investigated magnetic, charge, and transport properties of hexagonal graphene nanoflakes (GNFs) connected to two metallic leads. Both on-site U and long-range interaction effects in GNFs are taken into account. Using the functional renormalization group method we have calculated the average relative staggered magnetization, the average relative difference between the occupation of sublattices, and the linear conductance. The ground-state phase diagrams at half-filling are obtained for the GNF systems with realistic screened as well as the uniformly screened long-range Coulomb interactions. The obtained phase diagram in $(U/t, \epsilon_{nl}^{-1})$ coordinates, where the parameter ϵ_{nl} rescales the strength of the nonlocal interaction, is shared by three phases: the semimetal (SM), the spin-density-wave (SDW), and the charge-density-wave (CDW) phase.

First, we have analyzed the zigzag-edge GNFs with screened realistic Coulomb interaction of Refs. [13,44]. We showed that with increasing size of the GNF, the phase boundary between the SM and SDW phases shifts to higher (lower)

values of critical long-range (on-site) interaction strength. The transition line between the SM and CDW phases is almost linear in $(U/t, \epsilon_{nl}^{-1})$ coordinates and weakly depends on the GNF size. We have found that for the realistic long-range interaction parameters freely suspended GNFs are far from both SM-SDW and SM-CDW phase-transition boundaries and belong to the SM phase. The estimated critical values of the on-site interaction U_c^N, corresponding to the SDW instability for purely local interaction, agree well with the result of the DMFT approach for $N = 54$ [12] and the result of the DCA approach for $N = 96$ [9].

Then, for comparison, we have presented the ground-state phase diagram for the zigzag-edge GNF system with $N = 96$ and the uniformly screened Coulomb potential. For the SM-SDW phase transition, we have found moderate suppression of the critical long-range interaction strength in comparison to the one obtained for the realistically screened Coulomb interactions. In contrast, the transition line between the SM and CDW phases is rather different for the realistic and uniformly screened long-range Coulomb interactions. The realistic screening of the Coulomb interaction by σ bands causes a strong enhancement of the critical value of the long-range interaction needed to stabilize the CDW state. This results in a substantially wider region of stability of the SM phase for the case of the realistic nonlocal potential. In particular, the critical nonlocal interaction of the CDW phase at $U = 0$ is sufficiently larger for the realistic potential than the corresponding value for the uniformly screened potential. The latter value is consistent with the results of QMC in Ref. [24] and the mean-field approximation with dynamic renormalized Coulomb interaction [25,26]. The result on the SM-SDW transition line agrees well with the scaling analysis of QMC data [14].

Finally, we have shown that the behavior of the linear conductance G of the GNF system has a close connection with its magnetic or charge order. In particular, the linear conductance is strongly suppressed in both the SDW and CDW phases. The linear conductance as a function of ϵ_{nl} exhibits a peak for $U > U_c^N$, corresponding to the SM phase of the system. At the same time for $U < U_c^N$, when the SDW phase does not occur, the peak is absent and the conductance $G(\epsilon_{nl})$ shows a monotonous behavior.

Analysis of GNFs with armchair edges shows that for fixed local interaction U both SDW and CDW phase transitions for these systems take place at values of nonlocal interaction (higher ϵ_{nl}) somewhat smaller than those of the corresponding transitions in zigzag-edge GNFs with close N.

We emphasize that the present fRG study is limited to the case of an ideal (nondistorted) graphene lattice, and the Kekulé bond order phases [61,62] do not appear in the phase diagrams of GNFs. The possibility of these phases in GNFs can be also considered within the fRG approach when an initial small distortion of the hopping matrix elements between A and B sublattices, playing the role of symmetry-breaking perturbation, is introduced. Another important issue is the consideration of disorder effects, which may play a significant role in GNFs, as is the case for graphene [63–67]. The effects of disorder are expected to reduce the tendency towards charge and spin ordering in GNFs. A detailed analysis of these issues is beyond the scope of the present investigation but would be an interesting subject for future studies.

We also note that the results of the present paper are obtained at half-filling and for an equilibrium state of the GNF systems. However, the functional renormalization group method used in our study can be straightforwardly applied beyond both these limitations. In this perspective, investigation of magnetic and charge properties of GNFs for finite gate and bias voltages has to be performed. Apart from that, study of other carbon nano-objects, e.g., carbon nanotubes, is of certain interest.

ACKNOWLEDGMENTS

[1] Z. Luo, S. Kim, N. Kawamoto, A. M. Rappe, and A. T. C. Johnson, ACS Nano **5**, 9154 (2011).

[2] J. Güttinger, F. Molitor, C. Stampfer, S. Schnez, A. Jacobsen, S. Dröscher, T. Ihn, and K. Ensslin, Rep. Prog. Phys. **75**, 126502 (2012).

[3] I. Snook and A. Barnard, "Graphene nano-flakes and nano-dots: Theory, experiment and applications" in *Physics and Applications of Graphene—Theory*, edited by S. Mikhailov (InTech, Rijeka, 2011).

[4] O. V. Yazyev, Rep. Prog. Phys. **73**, 056501 (2010).

[5] M. Ezawa, Eur. Phys. J. B **67**, 543 (2009).

[6] A. H. Rozhkov, G. Giavaras, Y. P. Bliokh, V. Freilikher, and F. Nori, Phys. Rep. **503**, 77 (2011).

[7] K. A. Ritter and J. W. Lyding, Nat. Mater. **8**, 235 (2009).

[8] J. Fernández-Rossier and J. J. Palacios, Phys. Rev. Lett. **99**, 177204 (2007).

[9] W. Wu and A.-M. S. Tremblay, Phys. Rev. B **89**, 205128 (2014).

[10] A. Valli, A. Amaricci, A. Toschi, T. Saha-Dasgupta, K. Held, and M. Capone, Phys. Rev. B **94**, 245146 (2016).

[11] A. Valli, A. Amaricci, V. Brosco, and M. Capone, Phys. Rev. B **100**, 075118 (2019).

[12] A. Valli, A. Amaricci, V. Brosco, and M. Capone, Nano Lett. **18**, 2158 (2018).

[13] M. V. Ulybyshev, P. V. Buividovich, M. I. Katsnelson, and M. I. Polikarpov, Phys. Rev. Lett. **111**, 056801 (2013).

[14] H.-K. Tang, J. Leaw, J. Rodrigues, I. Herbut, P. Sengupta, F. Assaad, and S. Adam, Science **361**, 570 (2018).

[15] C. Honerkamp, Phys. Rev. Lett. **100**, 146404 (2008).

[16] S. Sorella, Y. Otsuka, and S. Yunoki, Sci. Rep. **2**, 992 (2012).

[17] F. F. Assaad and I. F. Herbut, Phys. Rev. X **3**, 031010 (2013).

[18] D. Hirschmeier, H. Hafermann, and A. I. Lichtenstein, Phys. Rev. B **97**, 115150 (2018).

[19] P. Buividovich, D. Smith, M. Ulybyshev, and L. von Smekal, Phys. Rev. B **98**, 235129 (2018).

[20] W. Armour, S. Hands, and C. Strouthos, Phys. Rev. B **81**, 125105 (2010).

[21] H. Leal and D. V. Khveshchenko, Nucl. Phys. B **687**, 323 (2004); D. V. Khveshchenko and W. F. Shively, Phys. Rev. B **73**, 115104 (2006).

[22] O. V. Gamayun, E. V. Gorbar, and V. P. Gusynin, Phys. Rev. B **80**, 165429 (2009).

[23] J. Wang, H. A. Fertig, and G. Murthy, Phys. Rev. Lett. **104**, 186401 (2010).

[24] J. E. Drut and T. A. Lähde, Phys. Rev. Lett. **102**, 026802 (2009); Phys. Rev. B **79**, 165425 (2009); **79**, 241405(R) (2009).

[25] D. V. Khveshchenko, J. Phys.: Condens. Matter **21**, 075303 (2009).

[26] O. V. Gamayun, E. V. Gorbar, and V. P. Gusynin, Phys. Rev. B **81**, 075429 (2010).

[27] J. Gonzalez, Phys. Rev. B **92**, 125115 (2015).

[28] A. Katanin, Phys. Rev. B **93**, 035132 (2016).

[29] M. Fujita, K. Wakabayashi, K. Nakada, and K. Kusakabe, J. Phys. Soc. Jpn. **65**, 1920 (1996).

[30] K. Szałowski, J. Magn. Magn. Mater. **382**, 318 (2015).

[31] M. Kabir and T. Saha-Dasgupta, Phys. Rev. B **90**, 035403 (2014).

[32] S. Ganguly, M. Kabir, and T. Saha-Dasgupta, Phys. Rev. B **95**, 174419 (2017).

[33] I. Hagymási and Ö. Legeza, Phys. Rev. B **97**, 035142 (2018).

[34] K. Luo and W. Sheng, J. Appl. Phys. **115**, 053705 (2014).

[35] Z. Shi and I. Affleck, Phys. Rev. B **95**, 195420 (2017).

[36] M. Raczkowski and F. F. Assaad, Phys. Rev. B **96**, 115155 (2017).

[37] A. Yamashiro, Y. Shimoi, K. Harigaya, and K. Wakabayashi, Phys. Rev. B **68**, 193410 (2003).

[38] L. Y. Zhu and W. Z. Wang, J. Phys.: Condens. Matter **18**, 6273 (2006).

[39] S. Chacko, D. Nafday, D. G. Kanhere, and T. Saha-Dasgupta, Phys. Rev. B **90**, 155433 (2014).

[40] H. Hadipour, E. Şaşıoğlu, F. Bagherpour, C. Friedrich, S. Blügel, and I. Mertig, Phys. Rev. B **98**, 205123 (2018).

[41] B. Wunsch, T. Stauber, F. Sols, and F. Guinea, Phys. Rev. Lett. **101**, 036803 (2008).

[42] W. Sheng, M. Sun, A. Zhou, and S. J. Xu, Appl. Phys. Lett. **103**, 143109 (2013).

[43] H. U. Özdemir, A. Altıntaş, and A. D. Güçlü, Phys. Rev. B **93**, 014415 (2016).

[44] T. O. Wehling, E. Sasioglu, C. Friedrich, A. I. Lichtenstein, M. I. Katsnelson, and S. Blügel, Phys. Rev. Lett. **106**, 236805 (2011).

[45] P. Buividovich, D. Smith, M. Ulybyshev, and L. von Smekal, Phys. Rev. B **99**, 205434 (2019).

[46] D. Smith and L. von Smekal, Phys. Rev. B **89**, 195429 (2014).

[47] M. Ezawa, Phys. Rev. B **77**, 155411 (2008).

[48] I. Weymann, J. Barnaś, and S. Krompiewski, Phys. Rev. B **85**, 205306 (2012).

[49] H. Şahin and R. T. Senger, Phys. Rev. B **78**, 205423 (2008).

[50] M. Salmhofer and C. Honerkamp, Prog. Theor. Phys. **105**, 1 (2001).

[51] W. Metzner, M. Salmhofer, C. Honerkamp, V. Meden, and K. Schönhammer, Rev. Mod. Phys. **84**, 299 (2012).

[52] C. Karrasch, T. Enss, and V. Meden, Phys. Rev. B **73**, 235337 (2006).

[53] A. P. Jauho, N. S. Wingreen, and Y. Meir, Phys. Rev. B **50**, 5528 (1994).

[54] F. Bauer, J. Heyder, and J. von Delft, Phys. Rev. B **89**, 045128 (2014).

[55] L. Weidinger, F. Bauer, and J. von Delft, Phys. Rev. B **95**, 035122 (2017).

[56] C. Karrasch, M. Pletyukhov, L. Borda, and V. Meden, Phys. Rev. B **81**, 125122 (2010).

[57] V. S. Protsenko and A. A. Katanin, Phys. Rev. B **94**, 195148 (2016).

[58] I. F. Herbut, Phys. Rev. Lett. **97**, 146401 (2006).

[59] The criterion $S_{st} = 1/4$ for the results of Ref. [13] is fulfilled for $\epsilon \approx 0.46$.

[60] We determine the critical local interaction $U_c(\epsilon_{nl} = \infty)$, which is needed to plot the results of Ref. [14] in units of U/t instead of U/U_c in the following way. We use that for $\gamma = 3\alpha/U = 0.5$ the critical interaction is $U_c = 4.2t$ (see Supplementary Material to Ref. [14]). This yields the corresponding $\alpha_c = 0.7$. Using further the analytic form of the SDW phase boundary $U_c(\alpha_0)/U_c(\alpha_0 = 0) = 1 + 0.06\alpha_0 + 0.14\alpha_0^2$ (see Supplementary Material to Ref. [14]), we find $U_c(\alpha_0 = 0) = 3.78t$.

[61] C. Gutiérrez, C.-J. Kim, L. Brown, T. Schiros, D. Nordlund, E. B. Lochocki, K. M. Shen, J. Park, and A. N. Pasupathy, Nat. Phys. **12**, 950 (2016).

[62] X. Y. Xu, K. T. Law, and P. A. Lee, Phys. Rev. B **98**, 121406(R) (2018).

[63] P. M. Ostrovsky, I. V. Gornyi, and A. D. Mirlin, Phys. Rev. B **74**, 235443 (2006).

[64] P. M. Ostrovsky, I. V. Gornyi, and A. D. Mirlin, Eur. Phys. J.: Spec. Top. **148**, 63 (2007).

[65] P. M. Ostrovsky, M. Titov, S. Bera, I. V. Gornyi, and A. D. Mirlin, Phys. Rev. Lett. **105**, 266803 (2010).

[66] A. Katanin, Phys. Rev. B **88**, 241401(R) (2013).

[67] B. Sbierski, K. A. Madsen, P. W. Brouwer, and C. Karrasch, Phys. Rev. B **96**, 064203 (2017).